Diurnal and seasonal results of the Schumann Resonance Observatory in Sierra de Filabres, Spain

Carlos Cano Domingo, Manuel Fernández Ros, Nuria Novas Castellano and José A. Gázquez Parra

***Abstract*—This paper presents the variations of the Schumann Resonances (SR), obtained in the Extreme Low Frequency (ELF) signal observatory of Sierra de Filabres belonging to the University of Almería, Spain, in operation since 2011. This station has two large and sensitive orthogonal sensors operating between 1 Hz and 100 Hz. A 24-bit low-noise, high-resolution system process the signal. The Sierra de Filabres ELF station is currently operating to offer interesting information on the activity of the Schumann Resonances in this area. This system allows us to have a broader range of comparison patterns, to study correlations with other phenomena. The information presented in this work deals with the diurnal and seasonal variations of the first six modes of the Schumann Resonances in 2016 and 2017. The graphs have been obtained through Lorentzian functions. We explain the diurnal variation based on the position and distance to the most important lightning hotspots and demonstrate its relation with the first mode captured in our observatory. We introduce a new yearly evolution method based on following the resonance frequency through the most representative lightning activity hours in one year. This paper is supported by the comparison between our signals and the global thunderstorm center's activity.**

***Index Terms*—Schumann Resonance modes, diurnal variation SR modes, seasonal variation SR modes, Extreme Low Frequency (ELF), lightning activity hotspot.**

I. Introduction

Schumann Resonances (SR) are global electromagnetic resonances produced within the earth-ionosphere cavity [1], [2]. These resonances appear due to electromagnetic excitation of the cavity mentioned above, at the frequencies where the interference is constructive [3]. Its resonant frequencies are mainly determined by the Earth's radius, speed of the light, and the earth-ionosphere cavity characteristics [4], including the ionosphere and Earth conductivity profile [5]. A first approximation of SR peaks can be calculated with Equation (1).

$$f_n = \frac{c}{2\pi a}\sqrt{n(n+1)}, n = 1,2,3,4\ldots \quad (1)$$

Where *n* represents the mode of the SR and *a* the Earth radius. Nowadays, approaches improving the accuracy have been proposed to consider that the Earth-ionosphere waveguide is not a perfect electromagnetic cavity.

Complex models consider the SR frequency peaks around 7.8, 14, 20, 26, 33, and 39 Hz for the first six modes of SR [6], [7], which are in the extremely low frequency (ELF) range [8]. There is a consensus that the SR's variation is mainly influenced by lightning activity [9] and the ionosphere state [10]. In order to describe how waves in the ELF range propagate, several models have been proposed. These intend to explain the earth-ionosphere cavity characteristic parameters, both analytical [11], [12], and simulated [13], [14].

This paragraph of the first footnote will contain the date on which you submitted your brief for review. The Ministry of Economics and Competitiveness of Spain financed this work, under Project TEC2014-60132-P, in part by Innovation, Science and Enterprise, Andalusian Regional Government through the Electronics, Communications, and Telemedicine TIC019 Research Group of the University of Almeria, Spain and in part by the European Union FEDER Program and CIAMBITAL Group. By I+D+I Project UAL18-TIC-A025-A, the University of Almeria, and the European Regional Development Fund (FEDER). We also thank the Andalusian Institute of Geophysics. The authors are with the Department of Engineering, University of Almeria, Almer´ıa 04120, Spain (e-mail: carcandom@ual.es; mfernandez@ual.es; nnovas@ual.es; jgazquez@ual.es)

Since lightning discharges arise continuously at any one time, extract a singular lightning stroke is not possible. However, averaging the Power Spectrum Density (PSD) is the most common approach for analyzing SR [15], [16].

The effect of the lightning global activity hotspot depends on the source-observer distant and position [7]. Recently, a study about the most important global lightning hotspots has been published [17]. The location and intensity variations of the most important global lightning activity centers are described in the study.

There are a vast number of papers describing experimental results in different locations of the world. A growing interest has been developing in the relation between different world events and their effects on SR parameters in recent years. To highlight some of them: connection with solar activity [18], association with the global temperature [19], and link with earthquake activity [20], [21].

For Schumann Resonances' study, the University of Almería developed the first ELF observatory in Spain in 2011. The system measures two orthogonal magnetic fields, North-South (NS) and East-West (EW), with a low noise instrumentation amplifier and 24 bits high-resolution analog-to-digital converter. The data obtained is preprocessed by a mean average filter and sent through a microwave transmitter to the server located at the University of Almería. The observatory is located in Sierra de Filabres (Lat. 37.1, Long -2.6), province of Almería, away from any human-produced electromagnetic interference (Fig. 1). Extensive and detailed information about the observatory features and performances can be found in [22].

Fig. Equipment of Sierra de Filabres ELF observatory, Almería.

The lower ionosphere conditions can change either due to regular variations or to sporadic events. Establishing how the former affects SR' parameters are not only crucial for understanding the signal but also essential to enable scientific advances in other disciplines by correlating them with natural events. That is why when the topic became relevant to the scientific community (mid-XX century), both theoretical and experimental studies focused on assessing diurnal and seasonal cycles on these parameters' fluctuation. Balser et al. (1962) [23] explained the relation between diurnal variation on the first mode averaged power and the average worldwide thunderstorm activity expected for a month. Chapman et al. (1964) [3] observed regular diurnal and seasonal changes over a period of one year in the first few resonant modes with an interpretation of the ionosphere model. Ogawa et al. (1969) [24] presents a diurnal variation comparison between experimental results and theoretical derivations, considering worldwide thunderstorms as noisy sources.

In the last few years, the number of ELF observatories over the world has increased overall. This increment has led to an expansion of Schumann resonances' available experimental data, focusing on diurnal and seasonal variations. Most of these studies analyze the deviation frequency and amplitude value of SR peaks.

Jagadish Rai et al. (2009) introduce a study of the SR frequency variations at Dharali (Himalayan region, India). It highlights the differences between the average spectral power for different day times (Sunrise, Noon, Sunset, and Night) for $\mathcal{E}_{NS,EW}$ and $\mathcal{B}_{NS,EW}$, with a significant difference between Noon and the rest. It depicts as well the daily evolution of the first two SR modes for $\mathcal{E}_{NS,EW}$ and $\mathcal{B}_{NS,EW}$ over a month [25].

Hongjuan Zhou et al. (2013) presents the diurnal variations of seasonally averaged mode amplitudes for the first four modes of $\mathcal{B}_{NS,EW}$. It shows frequencies' variation and evolution over one year. The data is obtained from two different ELF observatories located in China. Besides, the effect of the ionosphere cavity asymmetries is discussed. The asymmetries are based on the differences between the conductivity profile during day and night [26].

X. Y. Ouyang et al. (2015) show one year of data from four observatories located in China's low latitudes. The parameters have been processed using a Lorentzian fit over an ELF signal from 3 Hz to 29 Hz. The article presents the spectrogram of the first three modes for $\mathcal{E}_{x,y}$ and $\mathcal{B}_{x,y}$. However, the work's primary purpose is to highlight the differences in diurnal frequency and intensity peak values between the four seasons of the year [27].

Colin Price et al. (2016) analyses processed data from an observatory near Mitzpe Ramon in Israel. The components are extracted using a Lorentzian fit. The article presents the 4-year mean diurnal and seasonal variation of the SR peak for the first three modes for $\mathcal{E}_Z$ and $\mathcal{B}_{NS,EW}$ regarding frequency peak, relative intensity peak, and Q-factor peak [6].

G. Tatsis et al. (2020) analyses the diurnal variations on the first five modes, split by seasons and focusing on peak frequency, peak power, and Q-factor for $\mathcal{B}_{NS}$. The data has been obtained from an observatory located in the Northwest of Greece, and its characteristics are extracted using a Lorentzian fit. Furthermore, the paper also discusses the correlation between SR parameters and lightning activity, both global and local [28].

A. V. Koloskov et al. (2020) present an analysis involving a more extended period than usual. The paper explores the frequency and intensity variations on the first SR mode, working with data from distant observatories, one in the Antarctic and the other in the Arctic. The evolution over the period 2002-2018 can be observed in the article. Due to the difficulty of processing the vast amount of different data, the study calculated the total PSD of the horizontal magnetic fields. It presented clear evidence not only of the periodic yearly fluctuation but also of different tendencies depending on the latitude [29].

In this work, the results of acquiring, processing, and interpreting the data obtained in the previously mentioned observatory will be shown. This study's primary purpose is to highlight the diurnal and seasonal variations in the first six modes' SR peak frequencies. The research is done by analyzing measurements of the horizontal magnetic field $\mathcal{B}_{NS}$ and $\mathcal{B}_{EW}$ throughout 2016-2017. Section 2 briefly describes our observatory, data process algorithm, and our perspective on data interpretation. The results are presented in Section 3. Section 4 highlights the most prominent features and examines the interrelations with other works. Our conclusions are drawn in the final section.

II. Schumann Resonance Measurement

In this section, we introduce the different stages of the program for processing Schumann Resonance's measurements. A simplified diagram in Fig. 2 can be seen in which we summarized the different steps presented in this section.

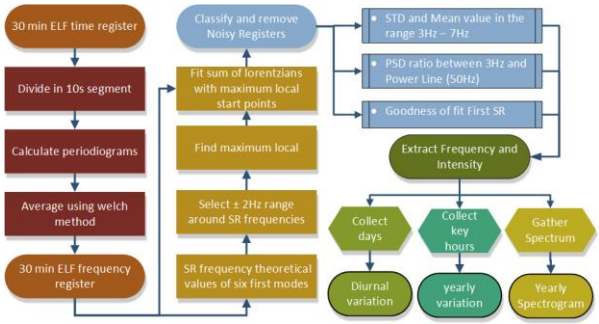

Fig. 2. Flow chart of the SR measurement.

The research group "Electronica Comunicaciones Y Telemedicina" developed the observatory that recorded the data used in this study at the University of Almería. It began to operate in 2011, being the first ELF measurement station in Spain and has been steadily improved ever since. The observatory is located in an isolated place in the Sierra de Filabres area, devoid of human interference to reduce background noise and electromagnetic interference.

The station is equipped as follows:

– Sensing stage: Composed of a couple of magnetic coils in orthogonal disposition, one with NS orientation and the other with EW orientation. These sensors were specifically designed and built for their purpose, and their characteristic curve has been obtained to calibrate the produced data [30].

– Conditioning stage: Based on a low noise and high gain amplifier and level scale adapter, it shows strong linearity in the range from 1 Hz to 100 Hz, which allows for a considerable number of SR modes to be appreciated in the data [16].
– Acquisition and processing stage: A two-channel, 24-bit Analog to Digital Converter (ADC) with delta-sigma modulation samples the data. Captured data is then further decimated by oversampling techniques, thus reducing the sample rate to 187 samples per second in order to minimize the acquisition noise. The data is then temporally stored until enough samples are captured to be sent.

A. Data processing algorithm

As the leftmost column in Fig. 2 illustrates, the processed data comes in 30-minutes files, each tagged with the date and time at the segment's start. Consequently, each day's worth of data has 96 files; two batches of 48 registers 30 minutes long, one for each magnetic field component. Each file is filtered using a high-pass filter with a lower cut-off frequency of 3 Hz to suppress the low-frequency components unrelated to SR.

For each 30-minutes file, its PSD is calculated. There are several proposed methods for calculating the PSD of the signal, although the tendency in recent papers has been using spectral averaging to reduce noise and increase resolution [31]. The most promising technique for our data is Welch's averaged periodogram method, following our research to optimize the algorithm [16]. Each 30 minutes register has 336600 data points; prior to the analysis, these registers are split into 10 seconds segments (1870 data points). Then the Fast Fourier Transform (FFT) is applied to each segment. The result of all FFTs is averaged to compose the 30 minutes PSD.

Due to the high sensibility of the magnetic coil sensor, any possible electromagnetic interference caused even by the wind's action on the ground may generate several undesirable artifacts in the output. Therefore, the data processor must account for methods in order to minimize interference impact. Averaging PSD produces a significant reduction, but these undesired components can be mitigated even further with the appropriate algorithm techniques. With that in mind, the chosen method for obtaining SR parameters was to fit the PSD using Lorentzian functions following Equation (2). This method was proposed in [32] and has been used by several authors for this purpose [33], [34], [35].

$$L(t) = \sum_{i=1}^{i=6} \left[\frac{Amplitude_i}{1 + (\frac{(t - Center_i)}{Width_i})^2} \right] + k \qquad (2)$$

As the second column in Fig. 2 shows, the parameter extraction process has four stages. First, the sixth lower modes' theoretical SR frequency values are considered to be applied to PSD data after a smooth filter. These two steps are combined in order to select local maxima on smoothed data around the theoretical SR frequencies values. The last stage is to fit the data to a sum of six Lorentzian functions, using each maximum relative point as a baseline to improve the fitting algorithm's accuracy. In order to ensure the quality of fit, the trend is removed in the fitting process.

As an example, Fig. 3 shows an SR register power spectrum, with the data produced by the Lorentzian fitting process overlaid (black line). The first six modes can be identified, showing how Lorentzian sums adjust an accurate representation even when the register has a strong noise component.

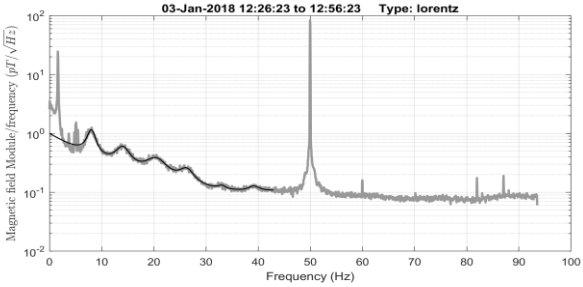

Fig. 3. Example of a $\mathcal{B}_{NS}$ spectrum of the Sierra de Filabres observatory using Lorentzian fit. Color black line shows the Lorentzian fit.

B. Data selection algorithm

Due to the station's characteristics and our observatory location, some registers present a strong noise component derived from the weather with substantial wind influence. Therefore, a layer of the analysis process oversees identifying and excluding these registers for the day-night and seasonal variation, as shown in the top right part of Fig. 2.

Weather disturbance presents a substantial effect in the ELF register's low band, mainly between 1 Hz and 10 Hz. In order to detect the presence of these phenomena, we proposed the following criteriums:

– The Standard Deviation (SD) on the lower locale of the first mode (3-7 Hz) as a representation of low-frequency disturbances, given the spikes it produces on the spectrogram.
– Mean value in the same range, accounting for the average power contributed to the spectra by the mentioned disturbances.
– Ratio between low frequency (3 Hz) and power line frequency (50 Hz) maxima, using the latter as a reference to evaluate the power condensed near the former.
– The goodness of fit is centered on the first mode in order to detect anomalies or registers whose fit does not seem accurate.

If a register fails to meet any of the mentioned criteria, the sample is rejected and excluded from the analysis process for all SR modes. The selection layer's result has a massive impact in Winter due to the weather condition in the observatory location.

C. Data interpretation

The aim of this study is to analyze patterns in the SR's characteristic parameters variation over time. A fundamental problem in the literature concerning this topic is that there is usually no established relation between different times. Most authors have focused on the differences between

data collected in different seasons and hours, looking for general differences. Although this approach is interesting, it fails to take into account the continuity over time between SR parameters at different intervals.

Within this purpose framework, the last part of the analysis process was developed (lower right part of Fig. 2). Through it, we obtain the evolution, differences, and periodicity of SR main parameters, the interval of analyzed data being from January 2016 to December 2017, with two sets of data, one for each horizontal magnetic field component.

This study is focused on the parameters of frequency and amplitude variation for the first six modes. Capturing and extracting SR parameters of the first six modes represents a groundbreaking achievement due to the high bandwidth needed to capture the ELF signal accurately. One of the significant drawbacks of SR studies is that most research is performed using signals where only the three or four first modes are captured with enough resolution. The analysis of the first six modes brings additional information for studying SR in comparison with other studies.

We have studied lightning hotspots that significantly impact our observatory, to relate our data with global lightning activity. Position and intensity variation shows that there is a spread map over all the world [17]. We can cluster them in three main zones: Asian, South-American, and African thunderstorm centers. Considering the source-observer position and distance, we summarize the most important thunderstorm centers in Table I. From the left column to the right, it shows the place, main reception magnetic component, higher flash rate time interval in UTC, and peak season activity.

TABLE I

MAJOR IMPACTING HOT SPOTS IN CALAR ALTO OBSERVATORY IN UTC[17]

	Magnetic field Component	Peak Activity (Hourly, UTC)	Peak Activity (Season)
Lake Maracaibo, VE	$\mathcal{B}_{NS}$	6:00 - 10:00	Spring Summer
Kabare, CD Kampene, CD Sake, CD	$\mathcal{B}_{EW}$	12:00 - 14:00	Winter Autumn
Patulul, GT	$\mathcal{B}_{NS}$	21:00 - 23:00	Spring Summer
Catarina, GT	$\mathcal{B}_{NS}$	21:00 - 23:00	Spring Summer
San Luis, CU	$\mathcal{B}_{NS}$	17:00 - 19:00	Spring Summer
Daggar, Pk	$\mathcal{B}_{NS}$	17:00 - 22:00	Spring Summer

III. RESULTS

Fig. 4 summarizes the data collected for the first six modes in the frequency domain and their time evolution.

The top row (Fig. 4a and 4b) shows the ELF spectrum of the $\mathcal{B}_{NS}$ component along each year, while in the bottom row (Fig. 4c and 4d), corresponds with the ELF spectrum of the $\mathcal{B}_{EW}$, the component can be observed during the same period. The green hue is related to higher values of intensity. These spectrograms clearly show the overall presence of the first three modes (the ones with higher intensity) around the theoretically expected frequency.

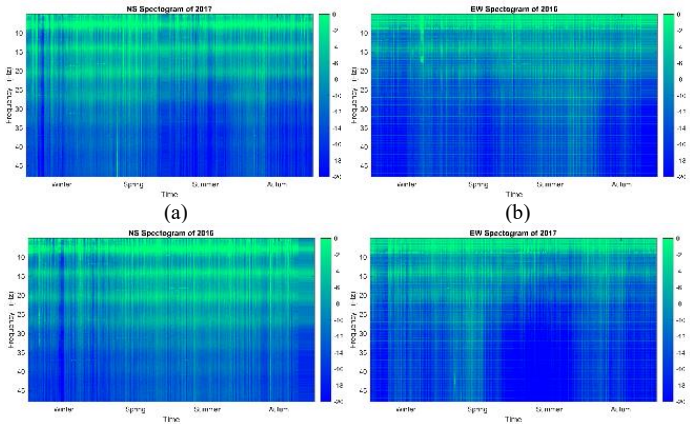

Fig. 4. Spectrogram of the $\mathcal{B}_{NS}$ (a) during 2016 and (b) 2017. Spectrogram of the $\mathcal{B}_{EW}$. (c) during 2016 and (d) 2017.

Since SR parameters' variations are related to changes in the earth-ionosphere cavity [5] and strongly correlated with global thunderstorm activity, it is expected to observe changes in its spectrum 24 hours of each day and also along different days. Due to the nature of the sensors, they are able to capture different kinds of electromagnetic phenomena with interest on their own. These are registered as a change of intensity in a short period of time, as can be observed in the spectrum.

A. Diurnal Seasonal Variation

SR varies along 24 hours in different ways along the four seasons. Frequency and intensity parameters are affected by this variation. Fig. 5 and 6 show variations of SR peak frequency for the first six modes, and Fig. 7 displays the evolution of SR peak intensity for the first three modes.

Regarding each set structure, the top row shows data collected in 2016, in the middle row, there are the data collected in 2017, and the average of both years is displayed in the bottom row. Each column corresponds to a different season (Jan-Mar for Winter, Apr-Jun for Spring, Jul-Sept for Summer, Oct-Dec for Autumn). The data format is the same for all graphs in every set; parameter of interest (frequency or intensity) along the Y-axis and time of the day in 24 hours format UTC, along the X-axis.

To assess daily average values through the season, the parameter of interest's values for a given time were averaged for every day on that season, providing the standard deviation. The black horizontal curve on all graphs represents the average value along 24 hours, and the grey area surrounding it represents a range of uncertainty proportional to the SD. The SD's magnitude is related to the number of registers that pass the data selection step and the average noise level.

Besides, four vertical lines have been included, representing the averaged time for different critical moments of the sun-cycle along one day, from left to right, Night, Sunrise, Noon, and Sunset, with the intention of emphasized the possible influence of the termination effect [36]. In the following subsection, frequency variation (1) and intensity variation (2) will be commented.

1) Frequency variation: Frequency variation on the first six modes of $\mathcal{B}_{NS}$ and $\mathcal{B}_{EW}$ are shown in Fig. 5 and 6.

The diurnal variation of $\mathcal{B}_{NS}$'s first mode can be seen in Fig. 5a. There are two crests and two troughs. The two crests are present at (05:30-08:30) UTC and (17:00-21:00) UTC in every season, with Winter's being the more stable around its maximum value. Of both troughs, Noon's (10:00-13:30) UTC is the more pronounced, whereas the midnight trough (22:00-2:00) UTC is less pronounced, with its downwards slope at the end of the day being appreciated only in Winter. Looking at the values averaged for both years, maxima and minima over the seasons are relatively consistent, with differences of tenths of mHz between seasons. Nonetheless, Spring-Summer minima are below Autumn-Winter's with the minimum value achieved in Summer (7.633 Hz). Of the two crests, the one happening around sunrise reaches the maximum value on every season, the average maximum between all seasons being 7.93 Hz, the highest of them all happening in Spring (7.95 Hz). The second crest's average through seasons reaches up to 7.86 Hz. The average values are also consistent between seasons, with an average yearly value of 7.81 Hz, which agrees with the usual frequency value for the SR first mode obtained experimentally in the literature, such as in the Barentzburg observatory [37].

The first mode for the other component $\mathcal{B}_{EW}$ is shown in Fig. 5b. In contrast with $\mathcal{B}_{NS}$ the SR frequency variation presents mainly one crest and one trough in Autumn and Winter, the former located around (12:00-14:00) UTC and the latter spanning mostly through the rest of the day. On the other hand, in Spring and Summer, a second crest appears after dusk, keeping a very stable value until rising in the Noon crest. This description comes from the fact that minimum values are also stable throughout the seasons (7.66 Hz), with the difference of Autumn-Winter minima happening around midnight. In contrast, Spring-Summer is around 18:00 UTC, between the two described crests. Maxima is also quite similar, with an average value of 7.93 Hz, with the highest value located in Summer, with 7.96 Hz. Lastly, the average values through seasons experiment a higher variation than in $\mathcal{B}_{NS}$, nonetheless negligible in absolute terms. The average yearly value is 7.77 Hz, with the maximum average belonging to Summer (7.82 Hz) and the minimum to Autumn (7.72 Hz).

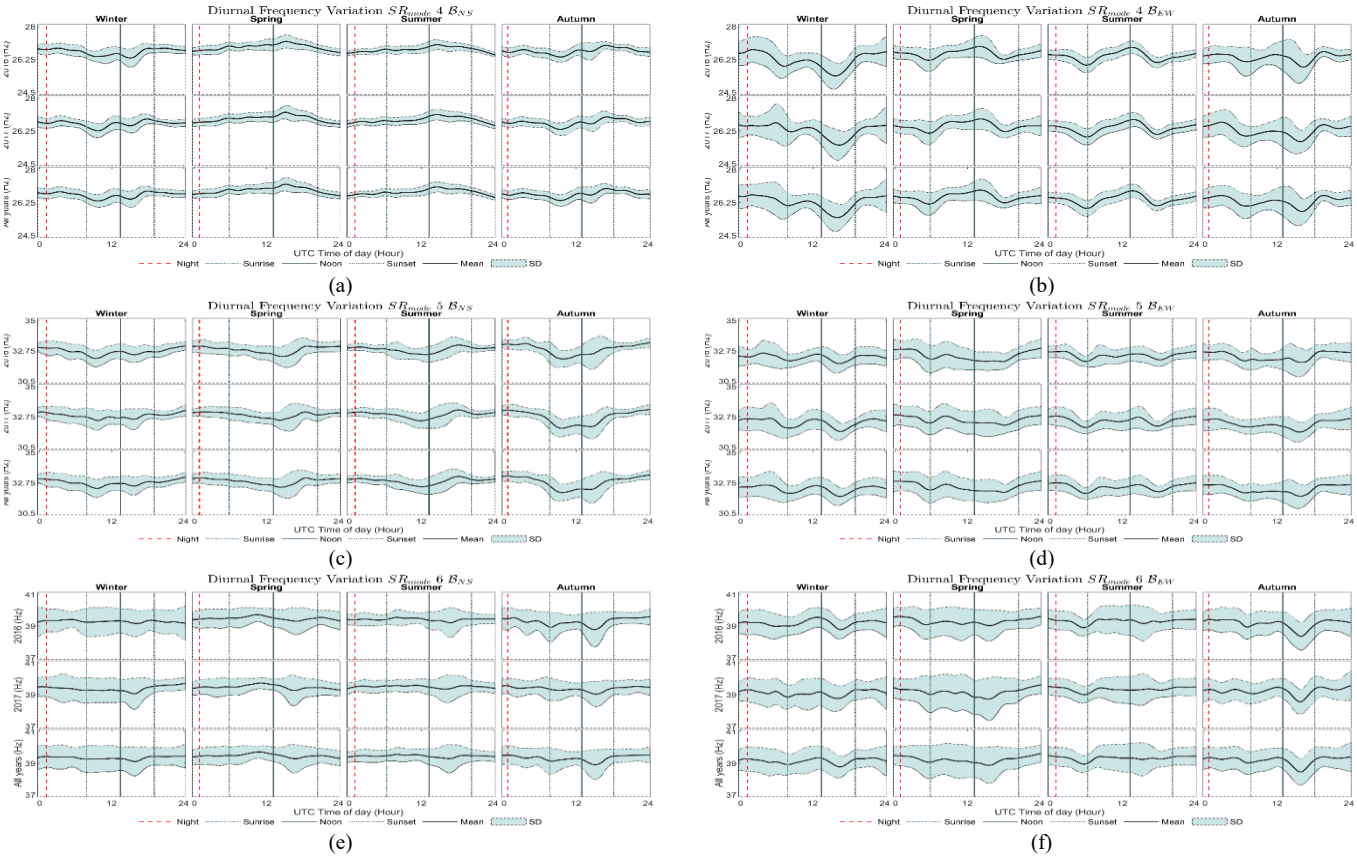

Fig. 5. Diurnal frequency variation of the $\mathcal{B}_{NS}$ during 2016, 2017, and averaged (24 hours) for the (a) first, (c) second, and (e) third SR modes. Frequency variation of the $\mathcal{B}_{EW}$. For the (b) first, (d) second, and (f) third SR modes.

Fig. 5c represents the frequency of the second mode of $\mathcal{B}_{NS}$. Regarding their general shape, all seasonal patterns display four maxima and four minima. Although their values change from one season to another, their position seems fixed around certain hours. It is worth highlighting a general trend during Autumn and Winter, making the line slightly U shaped, which is not present during Spring and Summer. Concerning the maximum values, the average throughout all seasons is 14.43 Hz. The difference in general trend between seasons causes the Autumn-Winter maxima to be located at 0:00 UTC, whereas in Spring-Summer, it is situated around 6:00 UTC. Minimum values are distributed in pairs; on Autumn-Winter, we find it on the second trough from the left around 10:00 UTC, while on Spring-Summer, it is located on the third trough,

around 15:00 UTC. The average minimum is 14.02 Hz. Lastly, the average values do not experience significant variations through seasons, with the total average being 14.23 Hz.

In Fig. 5d it can be seen the frequency variation of the second mode in $\mathcal{B}_{EW}$. Here, the presented signal shows two crests around Midnight and Noon and two troughs matched with sunrise and sundown.

Frequency variations along the day are more pronounced during Autumn-Winter than in the rest of the year. In the same fashion as in the $\mathcal{B}_{NS}$, minimum values are reached at different times during seasons, with Autumn-Winter minima being close to 6:00 UTC while during Spring-Summer, it is reached around 17:00 UTC. The minimal average value is 13.87 Hz. Maximum values are consistently reached during Noon throughout all seasons, around 12:30 UTC, with the average being 14.35 Hz. There is a small but clear difference between average values, with Autumn-Winter values being slightly higher (14.24 Hz) than in Spring-Summer (14.01 Hz). Not only their average values are superior during Autumn-Winter, but the range of values is also higher as well.

In Fig. 5e, the third mode of the $\mathcal{B}_{NS}$ channel can be observed. The signal shows a regular pattern during Spring and Summer with six crests and six troughs, while the number of these patterns is five in Winter and only four in Autumn. The most remarkable difference relative to the second mode of the same field component is the opposite behavior concerning the U shape. While Winter and Autumn show a flat trend, Spring and Summer display an inverse U shaped. The average value for all seasons is 20.27 Hz, with a slightly higher value during Spring and Summer. The minimum value during Winter and Autumn occurs around 10:00 UTC with a mean value of 20.01 Hz, while in Spring and Summer happens around 00:00 UTC with an average value of 20.12 Hz. Both this increment of variations in the number of crests and troughs and critical values are consistent with the other data obtained in the Nagicenk, Chambok, and Ipswich observatories [38].

Fig. 5f shows the evolution of the third mode for the $\mathcal{B}_{EW}$. Although a regular pattern along the year can be seen, the Winter season shows a high variability during daytime. The regular pattern between all seasons shows two troughs. The first happens consistently around 6:00 UTC, whereas the second comes to around 17:30 UTC. Minimum values come in the sunrise trough for every season, with an average value of 19.67 Hz.

Regarding maximum values, they are located around 13:30 UTC on every season, with slight differences (earlier in Autumn, and lately in Spring). Winter shows an odd behavior compared with the other seasons, pointing out to unaccounted phenomena. In the latter, the maximum frequency value is 20.12 Hz, where the rest ranges from 20.48 Hz in Spring-Summer and 20.62 Hz in Autumn. Average values are slightly lower in Autumn-Winter (20.24 Hz) than in Spring-Summer (20.34 Hz).

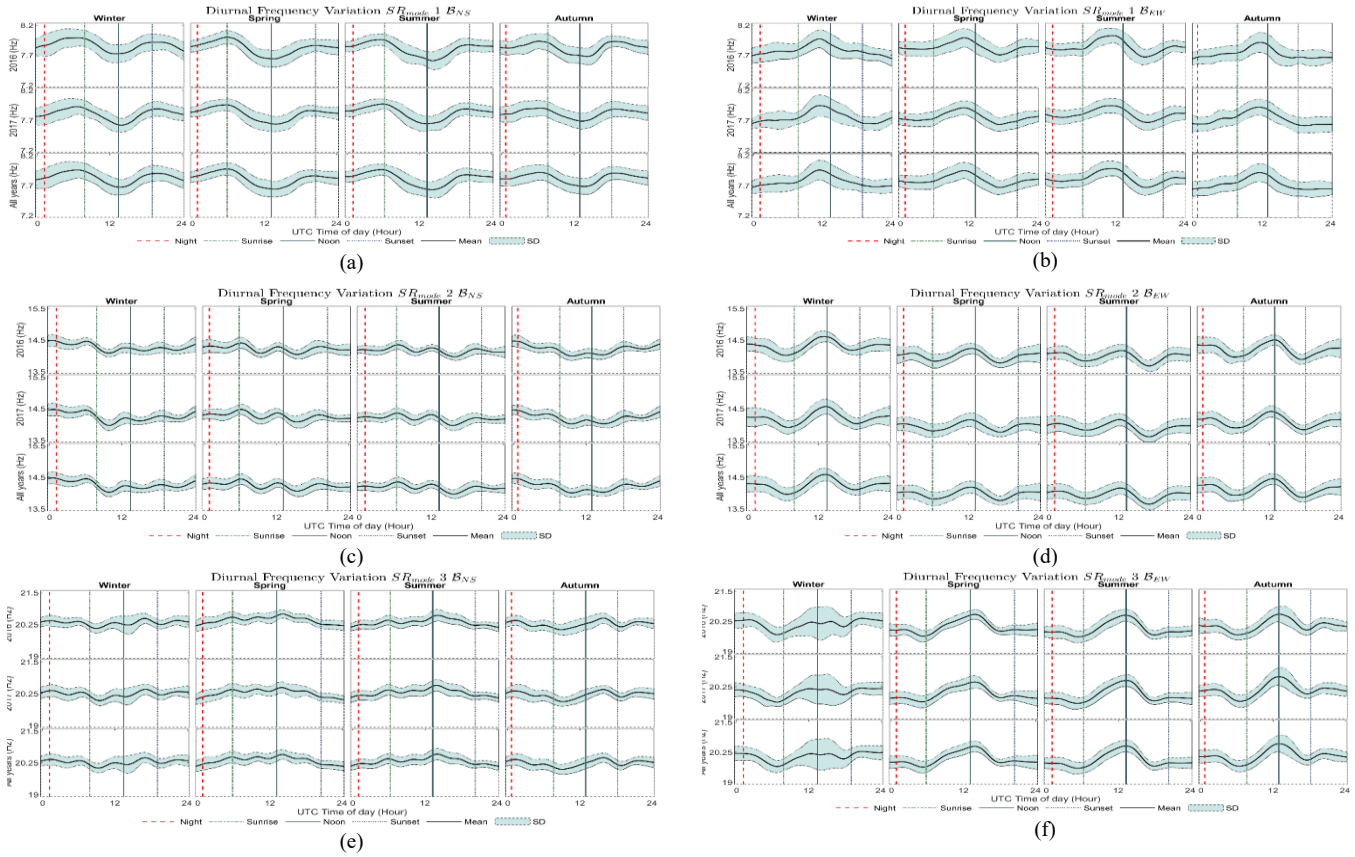

Fig. 6. Diurnal frequency variation of the $\mathcal{B}_{NS}$during 2016, 2017, and averaged (24 hours) for the (a) fourth, (c) fifth, and (e) sixth SR modes. Frequency variation of the $\mathcal{B}_{EW}$. For the (b) fourth, (d) fifth, and (f) sixth SR modes.

Fig. 6a shows the variation of the fourth mode for the $\mathcal{B}_{NS}$. The evolution is significantly different during Winter and Autumn, with two deep troughs followed each by one small crest. The first trough happens around 9:30 UTC with an average value of 26.30 Hz, while the second one is centered around 14:30 UTC with 26.54 Hz of the mean value of 26.54 Hz. In Spring and Summer, the pattern shows various crests and troughs with a strong crest near 15:00 UTC and a mean value of 27.10 Hz. Although the patterns are quite different from season to season, the average frequencies are nearly the same, with a total average of 26.71 Hz.

In Fig. 6b, the frequency variations of $\mathcal{B}_{EW}$ are depicted. There are two troughs in every season. The first is around 6:00 UTC, with an average minimum value of 26.10 Hz, while the second one is centered around 17:30 UTC, and its minimum average value being 26.10 Hz. Both troughs happen earlier during Spring and Summer, by one hour approximately. During Autumn and Winter, maximum values happen around 20:00 UTC, whereas, during Spring and Summer, they are located around 14:00 UTC. The latter pair has a mean maximum value of 26.82 Hz, while the former is 26.55 Hz. However, the average values along the year do not vary much, with 26.48 Hz.

In Fig. 6c, the evolution of the $\mathcal{B}_{NS}$ frequency variations for the fifth mode are shown. The observed pattern is quite different during the seasons. There are two big troughs around 9:30 UTC and 14:00 UTC in Winter and Autumn with an average minimum value of 32.40 Hz, significantly lower in Winter. In Spring and Summer, the pattern is a constant decreasing tendency from 00:00 UTC to 13:00 UTC and a significant slope that ends in a crest around 18:15 UTC where the maximum value (32.45 Hz) is reached. around 32.45 Hz. Throughout the year, the average value is mainly constant, with a value of 32.83 Hz, though higher values during Spring-Summer.

Fig. 6d shows the $\mathcal{B}_{EW}$ the counterpart for the fifth mode. The common pattern for this mode is two troughs. The first happens around sunrise for each season, reaching its minimum value at 6:00 UTC in Spring and Summer, at 7:00 UTC in Autumn, and 8:30 UTC in Winter. This trough is noticeably deeper in Winter, Spring, and Summer while being almost nonexistent in Autumn. The second trough minimum value is also reached at different times; Winter at 16:30, Spring and Summer around 18:00 UTC, and Autumn at 16:00 UTC. The minimum values for Autumn, Winter, and Spring happen during the second trough while Summer's minimum is in the first trough. Nonetheless, the values are quite similar, with an average minimum value of 31.93 Hz. The average value for the year is 32.36 Hz, with a difference of around 0.15 Hz between Autumn-Winter and Spring-Summer.

In Fig. 6e, the sixth mode resonance variations for $\mathcal{B}_{NS}$ are shown. The first thing to highlight is the SD value, which is overall higher than the rest of the modes. This SD value is due to the sixth mode's low power, making it difficult to provide an accurate fit in every case. Nonetheless, the average values confirm the general validity of the method, being 39.37 Hz. Regarding the pattern, a minimum value appears around 16:00 UTC, present in all seasons but especially noticeable during Autumn-Winter. The minimum value happens during Autumn, being 39.03 Hz.

Fig. 6f displays the $\mathcal{B}_{EW}$ resonance variations for the sixth mode, whose standard deviation is approximately the same as in its $\mathcal{B}_{NS}$ counterpart, and a slightly lower yearly average value of 39.20 Hz. Concerning its shape, the frequency values experience few variations during Spring and Summer, showing two troughs around 5:30 and 16:00 UTC. The former is slightly appreciable on Autumn and Winter, but the latter is deepened and preceded by a small crest. Once again, the minimum value appears in Autumn (38.39 Hz). On this particular SR mode, the trough between Noon and Sunset is different from any other. This trough is more pronounced on the $\mathcal{B}_{\mathrm{EW}}$ component, primarily through the colder seasons, and becoming less noticeable during summer. On the other hand, crests are less noticeable than in other modes, and it experiences a higher variation along the season, as shown by the gray area. Up to this point in the article, various distinct patterns have been appreciated on diurnal frequency variations.

2) Intensity variation: Intensity is a more complicated feature to compare since each electromagnetic effect (artifact or not) affects intensity. Nonetheless, a significant influence comes from the active storm centers at different hours as can be perceived clearly in Fig. 7, depicting intensity variations in the first three SR modes of the $\mathcal{B}_{NS}$ and $\mathcal{B}_{EW}$. The specific values for each mode are gathered in Table II.

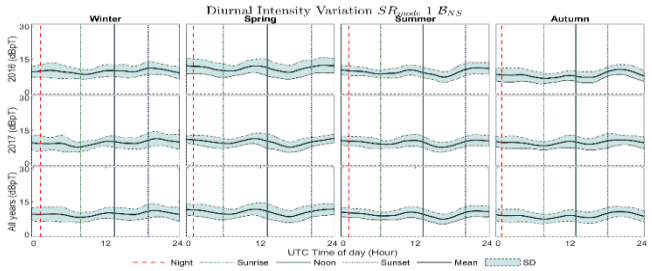

(a)

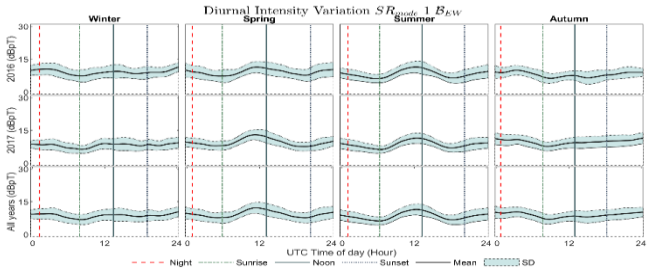

(b)

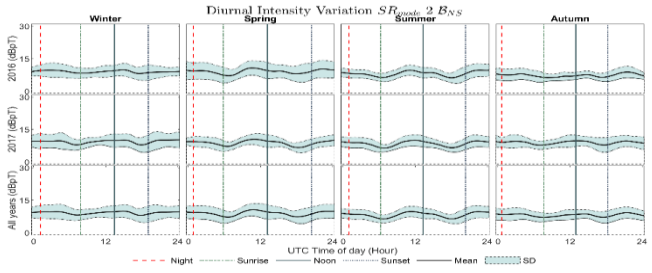

(c)

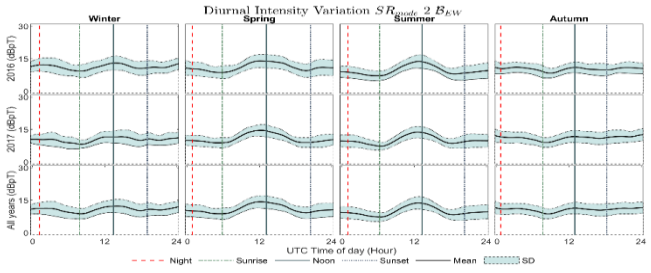

(d)

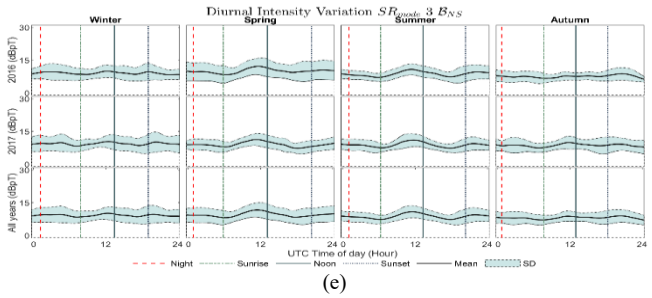

(e)

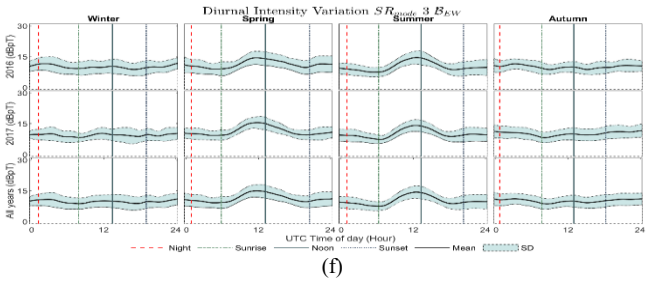

(f)

Fig. 7. The diurnal Intensity variation of the $\mathcal{B}_{NS}$ during 2016, 2017, and averaged (24 hours) for the (a) first, (c) second, and (e) third SR modes. Frequency Intensity of the $\mathcal{B}_{EW}$. For the (b) first, (d) second, and (f) third SR modes.

Table II

Hour and peak value of the trough in Intensity Variation along the average curve.

Mode		EW			NS						
		Maximum (12h)		Average	1st Maximum		2nd Maximum		3rd maximum		Average
		Time	Value (pT)	Value (pT)	Hour	Value (pT)	Hour	Value (pT)	Hour	Value (pT)	Value (pT)
1st SR	Winter	12:21	9.10	9.03			12:36	10.01	20.12	11.23	9.75
	Spring	11:20	11.84	9.68			11:18	11.67			10.59
	Summer	12:24	11.96	8.83			11:12	11.01			9.62
	Autumn	12:36	8.9	9.27	3:36	9.42	11:54	9.54	20:36	10.82	9.01
2ns SR	Winter	13:05	11.56	11.04	1:48	9.96	13:10	9.98			9.58
	Spring	12:06	13.88	11.19	2:54	9.55	10:48	10.75	22:00	10.28	8.68
	Summer	12:42	13.82	10.13			11:18	10.5	22:34	9.87	8.69
	Autumn	12:48	11.75	10.95	3:48	9.17	12:34	8.45	21:24	9.84	8.59
3rd SR	Winter	12:06	9.31	10.07	1:54	9.92	12:12	9.97	19:30	10.02	9.6
	Spring	11:30	14.27	11.55	2:48	9.77	11:30	11.61			9.81
	Summer	12:30	14.60	10.44			11:36	11.43			9.17
	Autumn	12:35	10.76	10.40	3:54	8.55	11:36	9.51	20:24	9.42	8.54

In the Intensity values for the first three modes on the $\mathcal{B}_{NS}$ magnetic component, three crests can be seen, whose maxima roughly fits the peak activity time from the three storm centers. These crests are clearly seen during Spring and Summer, while the third crest (evening) is visible throughout the year. The first crest is quite noticeable during Winter. Regarding the $\mathcal{B}_{EW}$ counterpart, the center crest is mostly present during Spring and Summer, being somewhat diminished in Autumn and Winter. In the last two seasons, the first crest (early morning) is noticeable.

B. Hourly Annual Variation

Annual frequency and intensity variations have been analyzed, as well. Its evolution is displayed in Fig. 8. Many authors have studied only frequency variations in the literature, and the study is done in one year with an all-day average peak frequency [29], [38]. This method's main limitation is that averaging diurnal variations' data to get yearly variations on a day-to-day basis may mask significant effects present only at certain hours. In line with this train of thought, we opted for a method based on selecting critical hours and follow the evolution of this hour along one year, shifting focus towards significant times of the day, applying it to frequency and intensity. The hours have been chosen based on their relation with lightning activity peaks, which will be discussed in Section 4. $\mathcal{B}_{NS}$ is more affected by the North American and Central Asian thunderstorm centers (7:00, 18:00, and 20:00 UTC) while $\mathcal{B}_{EW}$ is more affected by the African thunderstorm center (12:00 and 13:00 UTC) and slightly by the Southwestern part of the American center (7:00 UTC).

The behavior displayed in Fig. 8 for the mentioned magnitudes, and possible reasons will be explored in Section 4.

IV. Discussion

Overall, in the diurnal frequency variations presented in the last section, the most common conclusions are verified. The average values obtained match the typical experimental values for the different modes obtained in the works previously referenced. The higher values during Spring and Summer confirm the effect of the storm center's northward shift. In some modes, maximum or minimum values tend to coincide with the terminator, either sunrise or sunset, but this occurrence is, in our opinion, not common enough to be conclusive.

In order to support the discussion and how SR is firmly related to lightning activity, Fig. 8 is provided. It displays the activity of the most influential hotspots, given our observatory geographical location. The first two figures (Fig. 8a and 8b) shows the data related to $\mathcal{B}_{NS}$ and the seconds (Fig. 8c and 8d) to $\mathcal{B}_{EW}$.

Going into detail about $\mathcal{B}_{NS}$ frequency variations in the first mode, the two crests are due to the Asian and American thunderstorm centers' activity, whose peak activity matches the crests' time. The maximum values appear in the first crest (6:00 UTC, Asian center) rather than in the second (19:30 UTC, American center) regardless of the season. Since the latter is usually considered more potent than the former in terms of lightning contribution, this phenomenon shows the importance of source-observer distance and angle over total intensity. This pattern also matches the daily lightning activity displayed in Fig 8.a. Nonetheless, the pattern shifts in the rest of the modes, and a crest can be usually seen at Noon.

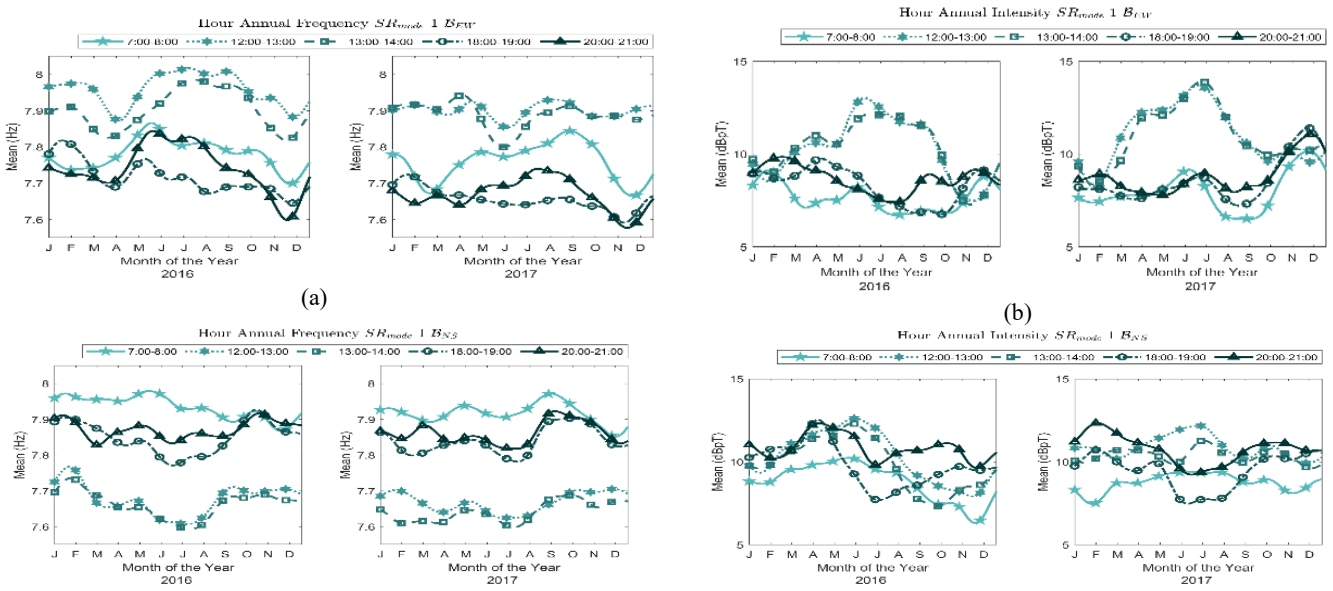

Fig. 8. Hourly Annual Frequency variation of the (a) $\mathcal{B}_{NS}$and (c) $\mathcal{B}_{EW}$ and Annual Intensity variation of the (b) $\mathcal{B}_{NS}$and (d) $\mathcal{B}_{EW}$ of the First SR modes during 2016-2017.

Concerning $\mathcal{B}_{EW}$, its pattern is quite more consistent along with different modes since the Noon crest is present in almost all. This crest is a consequence of the African thunderstorm center's peak activity during that time, as can be confirmed by Fig. 8c. Once again, the importance of distance over intensity is proven since Spring and Summer values are higher than in Autumn and Winter. As Fig. 8d confirms, hotspot activity is the opposite. Hence the factor responsible for this increase in magnitude must be the thunderstorm summer northward drift, which is consistent with the Nagicenk observatory shows in section 5.8 of [39].

As previously stated, SR's regular frequency variations are strongly related to the global lightning activity [23]. In particular, the SR is sensitive to lightning activity with continuing current [6]. Our results are congruent with the global lightning activity reported by [17], confirming specific lightning hotspots' prevailing effect at certain hours. Table I summarizes the major lightning hotspots affecting our observatory. How intense this influence is and which magnetic field component would register it is mainly explained by a geometrical factor depending on the relative position between the lightning source and the observatory [39]. However, other factors can alter the distribution [24].

The effect of lightning activity hotspot is also present in the Intensity variation figures. Table II shows the values of the maximum peak in both $\mathcal{B}_{EW}$ and $\mathcal{B}_{NS}$. It could be extracted clearly that the $\mathcal{B}_{EW}$ for the three first modes, the African thunderstorm is strongly affected by a peak around 12:00 UTC in Winter and Autumn. The intensity is over 2 pT over the mean value in these seasons, whereas in the other season are around the mean value. On the other hand, the $\mathcal{B}_{NS}$ is affected by more lightning hotspots with also a higher distance from our observatory. These data align with the data shown from the Kuju observatory in terms of shape [40]. In consequence, the maximum peaks are lower and more numerous. It is also clear that the affectation of the African thunderstorm is also present at 12:00 UTC.

Our data confirm a pattern relation between SR frequency variations in the first resonant mode and the most influential lightning hotspot in a given hour. Due to our observatory position, the ELF contribution by a specific lightning hotspot can be appreciated in only the components with a few exceptions, consistent with the previous assumption. It is also interesting that certain similarities between SR frequency variation trends and the lightning hotspot activity intensity of the most influential thunderstorm centers can be appreciated.

Fig. 9 shows frequency and intensity values for the first mode in key hours along both years. The hours have been selected to match the most active hotspots centers from Table I and depicted to perform comparisons between them.

We can observe how in Fig. 9a, the African thunderstorm center dominates in frequency contribution, showing the highest frequency values during its peak activity (from 12:00 to 14:00 UTC) by far. Although there is no apparent absolute resemblance between years, certain similarities in trend and average values can be appreciated. That being said, the trend followed by 12:00-13:00 UTC and 13:00-14:00 graph in 2017 is worth highlighting due to its similarity with African hotspots' annual activity. Considering the lack of activity outside peak hours (Fig. 8d) of the African thunderstorm center, the EW channel is sensitive to other lightning activity coming from different hotspots. The 7 to 8 hours line shows similarity with the annual evolution of Lake Maracaibo hotspot, as depicted in Fig. 8a. Given the angle and distance between this hotspot and our observatory (approx. 25º and 7500 Km, respectively), it is reasonable to think this channel can capture this activity.

In Fig. 9b, the African thunderstorm center's intensity clearly exceeds the contributed power at other hours due to its proximity to our observatory, remaining higher even in many months of less activity. Nonetheless, the fact of intensity peak values occurring in Summer, when the storm center is closer to our observatory, instead of Winter when its activity is higher, may indicate the relevance of source-observer distance over the actual lightning intensity.

Regarding Fig. 9c, the highest frequencies are given during the activity in Asia and America (7:00-8:00, 18:00-19:00, and 20:00-21:00 UTC). The trend similarities between years are higher than in the EW channel, which hints at reproducibility mainly in relative values.

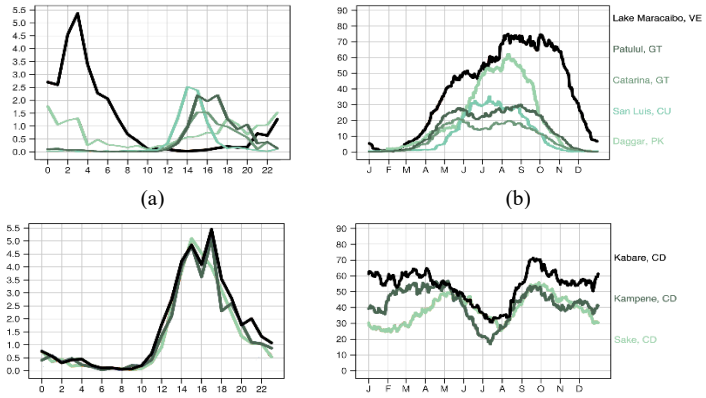

Fig. 9. Hourly and yearly evolution of the lightning activity in the most relevant lightning hotspot for the Calar Alto observatory [17].

Lastly, Fig. 9d present the intensities as received in the NS channel. As in Fig. 9c, similar trends are perceived between both years. Since African thunderstorm activity (parallel to the sensor) performs in the same range as the rest (orthogonal to the sensor), this points out again the importance of source-observer distance concerning intensity. Despite the range similarity, seasonal trends can be clearly perceived but also inverted in relation to each hotspot's peak activity season.

These results agree with previous findings in the literature [28], [29]. When lightning hotspots' activity is weak, the contribution from other factors has more impact on SR variation, thus increasing the variation range.

For computing a normalized value, we use the equations (4) and (5). The result is a measure of the frequency mean for a selected hour normalized with the variation for all hours.

We can see that the delta frequency variation is higher during key hours and decreases in the other hours, which can also be observed in figures 7a and 7c. The ratio is even more significant for the EW sensor, approximately by about 24%. This difference can be explained by the importance of the African thunderstorm center in the EW sensor compared to the NS sensor's primary lightning hotspot.

$$norm(x) = \frac{|mean(selected\ hour) - mean(all\ hours)|}{std(all\ hours)} \quad (3)$$

$$(\mathcal{B}_{NS})\ \frac{norm(\Delta F_{7:00,18:00,20:00})}{norm(\Delta F_{12:00,13:00})} = \frac{1.58}{0.74} = 2.16 \quad (4)$$

$$(\mathcal{B}_{EW})\ \frac{norm(\Delta F_{12:00,13:00})}{norm(\Delta F_{12:00,13:00})} = \frac{1.635}{0.61} = 2.67 \quad (5)$$

The comparison with other observatories supports the data we obtained and presented in this paper. To highlight the most important ones: Nagycenk (Hungary) [41], Moshiri (Japan), Letha (Russia), and West Greenwich (USA) [42]. Others comparison location has been introduced in the result section. Therefore, three recent papers with the same approach as this research will be presented.

G.Tatsis et al. (2020) present the diurnal evolution of the $\mathcal{B}_{NS}$ during 2016. The evolution of their data is very similar to our data about the $\mathcal{B}_{NS}$ component Fig. 5a, it is also important that the frequencies are higher during Autumn and Winter than in the rest of the seasons. However, the deviation from the theoretical SR frequency mode 1 differs due to the importance of distance [28].

X. Y. Ouyang et al. (2015) shows the diurnal variation of $\mathcal{B}_{NS}$ and $\mathcal{B}_{EW}$ during 2011 and 2012. For the first mode, the $\mathcal{B}_{EW}$ present the same behavior as our $\mathcal{B}_{NS}$. Moreover, the same can be said about the other magnetic component. It is less clear the similarities with our work in seasonal evolution. However, it could be explained by the geographical difference between the location of the observatories [27].

A. V. Koloskov et al. (2020) presents the evolution of the first SR mode from 2002 to 2020 in two different observatories. They focus on the average daily evolution along the different years. We can see a strong relationship during the year 2017 with the data we have obtained in our observatory for the same period in the $\mathcal{B}_{NS}$ component [29].

V. Conclusion

To sum up, we have confirmed the algorithm's utility and validity based on Lorentzian sum fitting supported by maximum local points to detect frequency and intensity variation of the first six modes of SR. The relationship between SR peaks' parameters obtained in Sierra de Filabres and others from similar studies has been confirmed, with locations spanning over the globe; Greece, South, Central America, South of China, the Arctic, and Antarctica. The not coincident patterns can be explained by the differences in latitude and differences in density and the recurrence of lightning activity. We also confirm the importance of the availability of worldwide published data in order to improve the studies about SR variation models and their application to studies about thunderstorm distribution and activity, ionosphere activity, and pre-seismic events detection. Finally, we have discussed the relationship between lightning hot-spots activity and first mode SR intensity and frequency at their peak activity hours. This discussion yields support to SR intensity depending on a source-observer relative position more than in total hotspot lightning discharge, with an angular position playing a role. The most active hotspot intensity of lightning discharge for a given hour has the most significant influence concerning frequency, with contribution from other hotspots masking it and the angle between source and observer affecting channel reception.

Finally, we also provided a new robust method for analyzing the evolution of SR frequency peak along one year based on selecting the hours when a thunderstorm center's influence is maximum on a particular magnetic component.

REFERENCES

[1] W. O. Schumann, "Über die strahlungslosen Eigenschwingungen einer leitenden Kugel, die von einer Luftschicht und einer Ionosphärenhülle umgeben ist," *Zeitschrift fur Naturforsch. - Sect. A J. Phys. Sci.*, vol. 7, no. 2, pp. 149–154, 1952, doi: 10.1515/zna-1952-0202.

[2] T. Madden and W. Thompson, "Low frequency electromagnetic oscillations of the Earth-ionosphere cavity," *Rev. Geophys.*, vol. 3, no. May, 1965, Accessed: Jan. 23, 2014. [Online]. Available: http://onlinelibrary.wiley.com/doi/10.1029/RG003i002p00211/full.

[3] F. W. Chapman and D. L. Jones, "Observations of earth-ionosphere cavity resonances and their interpretation in terms of a two-layer ionosphere model," *J. Res. Natl. Bur. Stand. Sect. D Radio Sci.*, vol. 68D, no. 11, p. 1177, 1964, doi: 10.6028/jres.068d.118.

[4] I. G. Kudintseva, S. A. Nikolayenko, A. P. Nickolaenko, and M. Hayakawa, "Schumann resonance background signal synthesized in time," *Telecommun. Radio Eng. (English Transl. Elektrosvyaz Radiotekhnika)*, vol. 76, no. 9, pp. 807–825, 2017, doi: 10.1615/TelecomRadEng.v76.i9.60.

[5] A. Tran and C. Polk, "Schumann resonances and electrical conductivity of the atmosphere and lower ionosphere-II. Evaluation of conductivity profiles from experimental Schumann resonance data," *J. Atmos. Terr. Phys.*, vol. 41, no. 12, pp. 1249–1261, 1979, doi: 10.1016/0021-9169(79)90028-X.

[6] C. Price, "ELF electromagnetic waves from lightning: The schumann resonances," *Atmosphere (Basel).*, vol. 7, no. 9, 2016, doi: 10.3390/atmos7090116.

[7] E. Prácser, T. Bozóki, G. Sátori, E. Williams, A. Guha, and H. Yu, "Reconstruction of Global Lightning Activity Based on Schumann Resonance Measurements: Model Description and Synthetic Tests," *Radio Sci.*, vol. 54, no. 3, pp. 254–267, 2019, doi: 10.1029/2018RS006772.

[8] ITU-R, *Nomenclature of the frequency and wavelengh bands used in telecommunications V Series Vocabulary and related subjects*, vol. 8. 2015.

[9] Abhijit Ghosh, D. Biswas, P. Hazra, G. Guha, and S. S. De, "Studies on Schumann Resonance Phenomena and Some Recent Advancements," *Geomagn. Aeron.*, vol. 59, no. 8, pp. 980–994, 2019, doi: 10.1134/S0016793219080073.

[10] I. G. Kudintseva, Y. P. Galuk, A. P. Nickolaenko, and M. Hayakawa, "Modifications of Middle Atmosphere Conductivity During Sudden Ionospheric Disturbances Deduced From Changes of Schumann Resonance Peak Frequencies," *Radio Sci.*, vol. 53, no. 5, pp. 670–682, 2018, doi: 10.1029/2018RS006554.

[11] T. Bozóki, E. Prácser, G. Sátori, G. Dálya, K. Kapás, and J. Takátsy, "Modeling Schumann resonances with schupy," *J. Atmos. Solar-Terrestrial Phys.*, vol. 196, no. October, 2019, doi: 10.1016/j.jastp.2019.105144.

[12] A. Kulak, J. Mlynarczyk, and J. Kozakiewicz, "An analytical model of ELF radiowave propagation in ground-ionosphere waveguides with a multilayered ground," *IEEE Trans. Antennas Propag.*, vol. 61, no. 9, pp. 4803–4809, 2013, doi: 10.1109/TAP.2013.2268244.

[13] J. J. Simpson and A. Taflove, "Two-dimensional FDTD modeling of impulsive ELF antipodal propagation about the earth-sphere," in *IEEE Antennas and Propagation Society, AP-S International Symposium (Digest)*, 2002, vol. 3, pp. 678–681, doi: 10.1109/aps.2002.1018302.

[14] J. J. Simpson and A. Taflove, "Three-dimensional FDTD modeling of impulsive ELF propagation about the earth-sphere," *IEEE Trans. Antennas Propag.*, vol. 52, no. 2, pp. 443–451, 2004, doi: 10.1109/TAP.2004.823953.

[15] B. Singh, R. Tyagi, Y. Hobara, and M. Hayakawa, "X-rays and solar proton event induced changes in the first mode Schumann resonance frequency observed at a low latitude station Agra, India," *J. Atmos. Solar-Terrestrial Phys.*, vol. 113, pp. 1–9, 2014, doi: 10.1016/j.jastp.2014.02.010.

[16] M. Fernández-Ros, J. A. Gázquez Parra, R. M. García Salvador, and N. N. Castellano, "Optimization of the periodogram average for the estimation of the power spectral density (PSD) of weak signals in the ELF band," *Meas. J. Int. Meas. Confed.*, vol. 78, pp. 207–218, 2016, doi: 10.1016/j.measurement.2015.10.006.

[17] R. I. Albrecht, S. J. Goodman, D. E. Buechler, R. J. Blakeslee, and H. J. Christian, "Where are the lightning hotspots on earth?," *Bull. Am. Meteorol. Soc.*, vol. 97, no. 11, pp. 2051–2068, 2016, doi: 10.1175/BAMS-D-14-00193.1.

[18] M. Sanfui and D. Biswas, "First mode Schumann resonance frequency variation during a solar proton event," *Terr. Atmos. Ocean. Sci.*, vol. 27, no. 2, pp. 253–259, 2016, doi: 10.3319/TAO.2015.12.02.01(AA).

[19] E. R. Williams, "The Schumann Resonance : A Global Tropical Thermometer," *Science (80-.).*, vol. 256, no. 5060, pp. 1184–1187, 1992, [Online]. Available: http://search.proquest.com/docview/213547553?pq-origsite=gscholar.

[20] K. Florios *et al.*, "Pre-seismic Electromagnetic Perturbations in Two Earthquakes in Northern Greece," *Pure Appl. Geophys.*, vol. 177, no. 2, pp. 787–799, 2020, doi: 10.1007/s00024-019-02362-6.

[21] J. A. Gazquez, R. M. Garcia, N. N. Castellano, M. Fernandez-Ros, A. J. Perea-Moreno, and F. Manzano-Agugliaro, "Applied engineering using Schumann Resonance for earthquakes monitoring," *Appl. Sci.*, vol. 7, no. 11, 2017, doi: 10.3390/app7111113.

[22] J. A. G. Parra, M. F. Ros, N. N. Castellano, and R. M. G. Salvador, "Techniques for Schumann Resonance Measurements: A Comparison of Four Amplifiers with a Noise Floor Estimate," *IEEE Trans. Instrum. Meas.*, vol. 64, no. 10, pp. 2759–2768, 2015, doi: 10.1109/TIM.2015.2420376.

[23] M. Balser and C. A. Wagner, "On frequency variations of the Earth-ionosphere cavity modes," *J. Geophys. Res.*, vol. 67, no. 10, pp. 4081–4083, 1962, doi: 10.1029/jz067i010p04081.

[24] T. Ogawa, Y. Tanaka, and M. Yasuhara, "Schumann Resonances and Worldwide Thunderstorm Activity: —Diurnal Variations of the Resonant Power of Natural Noises in the Earth-Ionosphere Cavity—," *J. Geomagn. Geoelectr.*, vol. 21, no. 1, pp. 447–452, 1969, doi: 10.5636/jgg.21.447.

[25] J. Rai, R. Chand, M. Israil, and S. Kamakshi, "Studies on the schumann resonance frequency variations," *Eur. Conf. Antennas Propagation, EuCAP 2009, Proc.*, pp. 1437–1440, 2009, Accessed: Jan. 23, 2014. [Online]. Available: http://ieeexplore.ieee.org/xpls/abs_all.jsp?arnumber=5067884.

[26] H. Zhou, H. Yu, B. Cao, and X. Qiao, "Diurnal and seasonal variations in the Schumann resonance parameters observed at Chinese observatories," *J. Atmos. Solar-Terrestrial Phys.*, vol. 98, pp. 86–96, 2013, doi: 10.1016/j.jastp.2013.03.021.

[27] X. Y. Ouyang, Z. Xiao, Y. Q. Hao, and D. H. Zhang, "Variability of Schumann resonance parameters observed at low latitude stations in China," *Adv. Sp. Res.*, vol. 56, no. 7, pp. 1389–1399, 2015, doi: 10.1016/j.asr.2015.07.006.

[28] G. Tatsis *et al.*, "Study of the variations in the Schumann resonances parameters measured in a southern Mediterranean environment," *Sci. Total Environ.*, vol. 715, 2020, doi: 10.1016/j.scitotenv.2020.136926.

[29] A. V. Koloskov, A. P. Nickolaenko, Y. M. Yampolsky, C. Hall, and O. V. Budanov, "Variations of global thunderstorm activity derived from the long-term Schumann resonance monitoring in the Antarctic and in the Arctic," *J. Atmos. Solar-Terrestrial Phys.*, vol. 201, no. February, p. 105231, 2020, doi: 10.1016/j.jastp.2020.105231.

[30] R. M. G. Salvador, J. A. G. Parra, and N. N. Castellano, "Characterization and Modeling of High-Value Inductors in ELF Band Using a Vector Network Analyzer," vol. 62, no. 2, pp. 415–423, 2013, doi: 10.1109/TIM.2012.2215141.

[31] C. D. Beggan and M. A. Musur, "Is the Madden–Julian Oscillation reliably detectable in Schumann Resonances?," *J. Atmos. Solar-Terrestrial Phys.*, vol. 190, no. December 2018, pp. 108–116, 2019, doi: 10.1016/j.jastp.2019.05.009.

[32] D. D. Sentman, "Magnetic elliptical polarization of Schumann resonances," *Radio Sci.*, vol. 22, no. 4, pp. 595–606, 1987, doi: 10.1029/RS022i004p00595.

[33] A. Guha *et al.*, "Aliasing of the Schumann resonance background signal by sprite-associated Q-bursts," *J. Atmos. Solar-Terrestrial Phys.*, vol. 165–166, no. April, pp. 25–37, 2017, doi: 10.1016/j.jastp.2017.11.003.

[34] R. Boldi, E. Williams, and A. Guha, "Determination of the Global-Average Charge Moment of a Lightning Flash Using Schumann Resonances and the LIS/OTD Lightning Data," *J. Geophys. Res. Atmos.*, vol. 123, no. 1, pp. 108–123, 2018, doi: 10.1002/2017JD027050.

[35] G. Sátori *et al.*, "Effects of Energetic Solar Emissions on the Earth–Ionosphere Cavity of Schumann Resonances," *Surv. Geophys.*, vol. 37, no. 4, pp. 757–789, 2016, doi: 10.1007/s10712-016-9369-z.

[36] A. Melnikov, C. Price, G. Sátori, and M. Füllekrug, "Influence of solar terminator passages on Schumann resonance parameters," *J. Atmos. Solar-Terrestrial Phys.*, vol. 66, no. 13-14 SPEC. ISS., pp. 1187–1194, 2004, doi: 10.1016/j.jastp.2004.05.014.

[37] V. C. Roldugin, Y. P. Maltsev, G. A. Petrova, and A. N. Vasiljev, "Decrease of the first Schumann resonance frequency during solar proton events," *J. Geophys. Res. Sp. Phys.*, vol. 106, no. A9, pp. 18555–18562, 2001, doi: 10.1029/2000ja900118.

[38] G. Satori, “Monitoring Schumann resonances--ll . Daily and seasonal frequency,” *Science (80-.).*, vol. 58, no. 13, pp. 1483–1488, 1996.
[39] A. Nickolaenko and M. Hayakawa, *Schumann resonance for tyros: Essentials of global electromagnetic resonance in the earth-ionosphere cavity*. 2014.
[40] A. Ikeda *et al.*, “Characteristics of Schumann Resonance Parameters at Kuju Station,” *E3S Web Conf.*, vol. 20, pp. 4–6, 2017, doi: 10.1051/e3sconf/20172001004.
[41] A. P. Nickolaenko, G. Sátori, B. Zieger, L. M. Rabinowicz, and I. G. Kudintseva, “Parameters of global thunderstorm activity deduced from the long-term Schumann resonance records,” *J. Atmos. Solar-Terrestrial Phys.*, vol. 60, no. 3, pp. 387–399, 1998, doi: 10.1016/S1364-6826(97)00121-1.
[42] A. P. Nickolaenko, E. I. Yatsevich, A. V. Shvets, M. Hayakawa, and Y. Hobara, “Schumann-resonance records at three observatories and ULF universal- and local-time variations,” *Radiophys. Quantum Electron.*, vol. 53, no. 12, pp. 706–716, 2011, doi: 10.1007/s11141-011-9263-y.